
Extended Buoyancy-Drag Model for Ablative Rayleigh-Taylor Instability Seeded by Various Perturbations

Dongxue Liu,¹ Tao Tao,¹ Jun Li^{1,3}, Qing Jia¹, Rui Yan^{2,3}, and Jian Zheng^{1,3,*}

- 1 (Department of Plasma Physics and Fusion Engineering, University of Science and Technology of China, Hefei 230026, People's Republic of China)
- 2 (Department of Modern Mechanics, University of Science and Technology of China, Hefei 230027, People's Republic of China)
- 3 (Collaborative Innovation Center of IFSA, Shanghai Jiao Tong University, Shanghai, 200240, People's Republic of China)

Email: jzheng@ustc.edu.cn

In inertial confinement fusion (ICF), affected by non-steady ablation and various physical mechanisms, we extend the classical buoyancy-drag (BD) model into an ablative version for evaluating and controlling nonlinear ablative Rayleigh-Taylor instability (ARTI) in real space. The application of our ablative BD model in the nonlinear phase lies in a single adjustable coefficient influenced by initial perturbations, linear growth rate and terminal velocity. After validating the effectiveness and sensitivity of this model through simulations, we propose a strategy to shift the dominant mode away from the "most dangerous mode", k_α , which depends on initial perturbations. Our findings suggest that k_α may clarify gain differences among targets of similar qualities and provide guidance for target manufacturing and pulse optimization in proximity to the ignition cliff.

Key words: buoyancy-drag model, ablative Rayleigh-Taylor instability, most

dangerous mode

1. Introduction

Inertial confinement fusion (ICF) aims to achieve ignition [1, 2], a milestone that remains a significant challenge primarily due to the influence of hydrodynamic instabilities [3, 4]. Among these instabilities, ablative Rayleigh-Taylor instability (ARTI) is particularly important, as it can evolve from a linear phase into a nonlinear phase during the acceleration phase. Nonlinear ARTI can lead to interpenetration or mixing between the hot, low-density ablator and the cold, dense ablator or fuel, forming bubbles that penetrate the implosion shell. Bubbles have been a contributing factor to the yield-over-clean (YOC) of less than 0.01 in early ignition experiments conducted during the National Ignition Campaign (NIC) [5-7] and have recently been implicated in gain discrepancies [8, 9] among targets and lasers of similar qualities. Previous studies have demonstrated that target defects and laser imprint [10, 11] can evolve into a nonlinear phase [12, 13], specifically a self-similar phase [14-17]. However, a straightforward growth model for evaluating and controlling multimode ARTI from the linear phase to the self-similar phase in real space is still lacking.

The foundational theories of ARTI across various phases can be summarized as follows. In the linear phase, a single mode grows exponentially until reaching an amplitude about 1/10 to 1/5 of its wavelength. The linear growth rate shapes like $\gamma \cong \sqrt{A_t k g} - \beta k v_a$ [18, 19], where v_a , g , k , A_t and β are the ablative velocity, acceleration, perturbation wave number, Atwood number, and a factor that depends on the heat conduction power index ν , respectively. In the nonlinear phase, the single mode achieves a terminal velocity, $U_B \sim C \sqrt{g A_t \lambda / 2}$ [20], where C denotes a constant and λ represents perturbation wavelength. For a full spectrum of perturbation modes, Hann [21] proposes that nonlinear behavior initiates when the

cumulative amplitude of modes within a specified wavenumber range becomes comparable to a wavelength, thereby allowing the wave packet to be approximated as a single mode, which has been validated experimentally [17]. Furthermore, Hann's weakly nonlinear theory for broadband ARTI [22], which incorporates γ into a classical second-order expansion, demonstrates that ablation can effectively mitigate the nonlinear growth rate. Since high-order expansions are inadequate for resolving the evolution of highly nonlinear ARTI, based on Hann's work, Dimonte [23] has proposed a method to derive a self-similar coefficient that describes the bubble depth h_B in a self-similar manner as the dominant wavelength increases during the subsequent self-similar phase. Nevertheless, the calculated self-similar coefficient varies due to non-steady ablation and complex physics inherent to ICF, indicating that the system is transiting towards a self-similar phase. To evaluate h_B during this phase, the classical buoyancy-drag (BD) [24, 25] model, which can be derived from Layzer's potential flow model [26], provides a valuable framework.

Originally proposed by Young [27] as a forcing equation for bubble dynamics, the BD model is adaptable due to several coefficients with physical connotations. In scenarios where $A_l = 1$, Layzer's model simplifies to a form: (mass + added mass) \times acceleration = buoyancy – drag, detailed as follows,

$$(1 + E) \frac{dV_B}{dt} = (1 + E) g - \frac{C_d}{R} V_B^2,$$

where, $V_B = \frac{dh_B}{dt}$ represents the bubble velocity; R relates to h_B ; and an exponential term E , applicable only in the small amplitude linear phase is omitted during the nonlinear phase. While both inertia and buoyancy are volumetric, drag is proportional to the cross-sectional area, incorporating a drag coefficient relevant to C_d . The added

mass associated with bubble shapes arises from the movement of the penetrated fluid. Several extended models have been proposed, such as modifying the drag coefficient of the classical BD model through transport coefficient to predict spikes at the interface of the hot spot [28] and incorporating an ablative stabilization term [29], analogous to the drag term, to better capture the dynamics of bubbles influenced by radiative shocks. However, these models often inadequately account for diverse physical mechanisms [30-35] relevant to ARTI in ICF.

In this paper, to describe the ARTI's nonlinear growth from a weakly nonlinear phase to a self-similar phase, we extend the classical BD model to develop an ablative BD model by enhancing the drag coefficient from a constant to one that encompasses various physical mechanisms. We employ simulations to assess the effectiveness and sensitivity of our ablative BD model in ICF. Subsequently, we propose shifting the dominant mode away from the "most dangerous mode", which depends on initial perturbations, to effectively control nonlinear ARTI. This mode provides a practical guidance for target manufacturing and pulse optimization, particularly as the National Ignition Facility (NIF) seeks to enhance the maximum target gain through improved target quality [36].

The paper is organized as follows. In Section 2, we extend the classical BD model to an ablative BD model. Validations of the model and its further application in guiding the control of nonlinear ARTI are presented in Section 3. Finally, we draw our conclusions in Section 4.

2. The extended ablative buoyancy-drag (BD) model

The classical BD model has been applied to weak nonlinear phase and its subsequent phases [37, 38] to describe the forcing of bubbles as shown in figure 1. Various drag coefficients, typically expressed as follows,

$$D \sim C_d \frac{\rho_B}{\rho_S + \rho_B} \frac{h_B}{\lambda_B} \quad [25],$$

are utilized during various phases, where ρ_B , ρ_S and λ_B denote time-varying quantities of bubble density, spike density and bubble wavelength, respectively. Therefore, we aim to extend the classical BD model to an ablative BD model to address the non-steady ablation scheme inherent in ICF which encompasses multiple physical mechanisms.

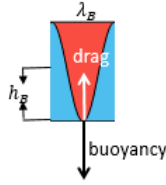


Figure 1. Forcing of a bubble with red indicating low-density fluid and blue representing dense fluid.

D is approximately constant during the weakly nonlinear and self-similar phases since experimental results have shown that the average h_B / λ_B and ρ_B / ρ_S [17] remains invariant within a stable-ablation scheme. Consequently, we can use the specific self-similar growth rate to derive the expression for D within this stable-ablation scheme. Following Hann's theory[21], which describes a full mode spectrum centered around a dominant mode, and Fermi's nonlinear transition [26], which indicates that a single-mode perturbation experiences exponential growth during the linear phase until reaching its terminal velocity U_B [20], as well as Birkhoff's approach [39] for obtaining the self-similar evolutions of the dominant bubbles by seeking λ_B that maximizes h_B , the self-similar coefficient under bubble competition scheme, expressed as follows, has been derived [23] and validated by simulations [14],

$$\begin{aligned}
\alpha_{ab} &= \left(\gamma_{k,0} / \sqrt{A_t k_{B,0} g} \right) \frac{C\sqrt{\pi}}{4} \left(\ln \left(\frac{U_{B,0}}{\langle h_{k,0} \rangle \gamma_{k,0}} \right) - 1 \right) \\
&= \left(1 - \beta \sqrt{k_{B,0} / (A_t g)^{v_a}} \right) \frac{C\sqrt{\pi}}{4} \left(\ln \left(\frac{C\sqrt{\pi}}{k_{B,0} \langle h_{k,0} \rangle (1 - \beta \sqrt{k_{B,0} / (A_t g)^{v_a}})} \right) - 1 \right)^{-1}, \tag{1}
\end{aligned}$$

where $\langle h_{k,0} \rangle$ represents the initial perturbations. To get the self-similar growth of h_B [23],

$$h_B = \alpha_{ab} A_t \left(\int \sqrt{g} dt \right)^2, \tag{2}$$

from Youngs's BD model,

$$\frac{dV_B}{dt} = A_t g - D \frac{V_B |V_B|}{h_B}, \tag{3}$$

we derive the expression of D by substituting equation (2) into (3),

$$D = \left(\frac{1}{\alpha_{ab}} - \frac{2s}{s+2} - 2 \right) / 4, \tag{4}$$

where $g \sim t^s$, ($s \geq 0$), $s = 0$ equals stable-ablation. Consequently, the ablative BD model is articulated using equation (3) with equation (1) and (4). If D is calculated with a constant g while h_B evolves with a time-varying g , h_B will be underestimated for $s > 0$ due to a larger D .

Regarding a non-steady ablation scheme, various physical mechanisms, including ablation, non-local electron heat transport, hot electron preheating, and self-generated magnetic fields, influence the growth of ARTI in two primary ways: γ and U_B [32] [35]. Consequently, the history of ablative acceleration and related physical processes can be incorporated through variations in γ and U_B as indicated in equation (1).

To evaluate h_B , determining the initial dominant perturbation is essential for calculating D and initiating equation (3). Given that the spectrum of initial

multimode perturbations in ICF may consist of several wave packets, based on Hann's study, we conceptualize these spectrums as a combination of distinct wave packets, each centered around its respective dominant wavelength. The wave number of the dominant perturbation can be extracted from the simulated density distribution at the

onset of acceleration, $k_{B,0} = \frac{\int \rho_{k0}^2 dk}{\sum \rho_{k0}^2}$. However, $\langle h_{k0} \rangle$ is notably small, ranging from

10^{-8} cm to 10^{-5} cm [23], necessitating alternative methods for its determination. The

perturbation velocity at the onset of acceleration is taken as $v_{k0} = U - \langle U \rangle$ [40] and

the initial perturbation amplitude is expressed as $\langle h_{k0} \rangle \approx v_{k0} / \gamma$, where U represents

local fluid velocity and $\langle U \rangle$ denotes mean fluid velocity. With these initial

perturbations, as well as data from one-dimensional simulations, specifically $v_a(t)$, A_t

(t), $g(t)$, $\beta(t)$, the predicted h_B during nonlinear phase can be validated through

following simulations.

3. Validation and application of the model via simulations

3.1 Simulation settings

In this study, we employ two-dimensional Eulerian radiation-hydrodynamic code

named FLASH [41] to evaluate the effectiveness and sensitivity of the ablative BD

model represented by equation (3) in ICF. The key simulation settings are as follows.

The lengths of the simulation domain in the X and Y directions are denoted as

$L_x = [-100\mu m, 100\mu m]$ and $L_y = [-400\mu m, 2000\mu m]$, respectively, with a spatial

resolution of $0.52\mu m$. The laser pulse ^{a)}, vertically irradiating the planar target, is a

square pulse with a rise time of 0.1 ns and a peak intensity of $25\text{TW}/\text{cm}^2$. The CH

planar target is set with a density of 1g/cc and a thickness of $90\mu m$. For the seeding

sources of multi-mode velocity perturbations adjacent to the surface, we define them as

$V_p(x) = \sum V_{pk} \cos(mk_L x + \psi_{k0})$, $k_L = 2\pi / L_x$, where m is an integer ranging from 4 to 10, ψ_{k0} is a random phase uniformly distributed between zero and one, $V_{pk} = V_{pk0} e^{(-mk_L|y-y_0|)}$, $V_{pk0} = F(mk_L)^{-2}$, and F is a constant. Table 1 displays the information of non-ideal simulations, which encompass the process of laser energy deposition, electron heat conduction, and heat exchange between electrons and ions, while excluding radiation transport effects. For case 1 at $t = 3.4$ ns, $V_p(x)$ has been loaded onto the target and a shock wave propagates through the rear interface of the target at $Y = 0 \mu m$, leading to the rapid growth of perturbations. Figure 2(a) and 2(b) illustrate the density distribution at the same time and position of the rear interface, highlighting the differences between the density profiles without and with the perturbations.

case	pulse	$\langle h_{k0} \rangle \approx v_{k0} / \gamma$ (10^{-7} cm)	$k_{B,0}$ (10^3 cm^{-1})	control of independent variables
1	a)	2.33	2.43	
2	b)	2.33	2.43	1→2: pulse ^{a)} to pulse ^{b)}
3	c)	10.00	2.94	
4	d)	10.00	2.94	3→4: pulse ^{c)} to pulse ^{d)}
5	a)	6.62	2.33	1→5: random
6	a)	10.40	2.26	1→6: deliberate
7	a)	23.00	2.38	1→7: deliberate
8	a)	16.00	2.73	
9	a)	16.80	4.95	8→9: deliberate
10	a)	14.30	2.17	9→10: deliberate
11	c)	10.00	2.94	3→11: $f=0.06$ to $f=0.04$
12	c)	10.00	2.94	3→12: $f=0.06$ to $f=0.1$

Table 1. The information of simulation cases with perturbations, where ‘deliberate’ represents modifying the initial perturbations with F and m , while ‘random’ denotes modifying the initial perturbation with random phase.

3.2 Effectiveness of the model

In comparison to figure 2(a), the multi-mode velocity perturbations in figure 2(b) lead to significant deformation of the planar target, exhibiting nonlinear characteristics

at $t = 10 \text{ ns}$. The low-density fluid penetrates the dense fluid, resulting in the formation of bubbles, while the dense fluid penetrates the low-density fluid, forming spikes. The interface between the bubbles and the spikes is defined as the outer edge of the accelerated shell, represented by the average position with $1/e$ of the peak density near the coronal region. The bubble front is expressed as $\min(\min(\nabla_Y \rho(X, Y)))$, and the spike front is denoted by $\max(\max(\nabla_Y T_e(X, Y)))$, where T_e represents the electron temperature.

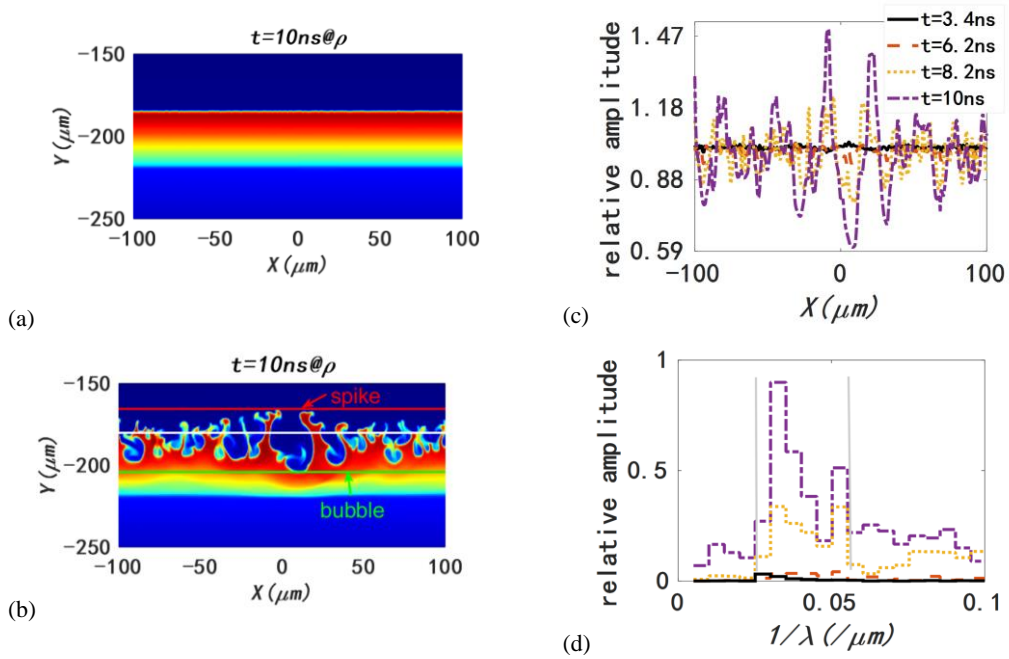


Figure 2. Distribution of density ρ for cases with (b) and without (a) velocity perturbations at 10 ns, where the red, white and green lines represent the spike front, the boundary between the spikes and the bubbles and the bubble front, respectively. (b) has clear nonlinear characteristics – the bubbles and the spikes. The spatial distribution (c) and Fourier spectrum (d) of ρ in X after summed in Y . The black solid lines correspond to the initial perturbations with their spectrums bounded by two gray lines in (d). The colors and the line styles are the same in (c) and (d). The dominant perturbation wavelengths at $t = 10 \text{ ns}$ are identical as those of the initial, demonstrating that bubble competition drives the evolution of the bubble front.

Figure 2(c) and 2(d) illustrate the evolution of bubbles in both real and spectral space to validate the bubble competition. The black solid lines represent the initial

perturbations, with their spectrums bounded by two gray lines in figure 2(d), at the onset of acceleration ($t = 3.4 \text{ ns}$). From $t = 3.6 \text{ ns}$ to $t = 6.2 \text{ ns}$, the initial perturbations with smaller wavelengths exhibit faster growth. Upon entering the nonlinear phase at $t = 6.2 \text{ ns}$, the initial perturbations with larger wavelengths begin to dominate due to competitive interactions among bubbles, leading to the phenomenon where one bubble expands while its neighbors shrink. Although perturbations with wavelengths exceeding the initial perturbation wavelengths emerge due to bubble merging, bubble competition continues to dominate the evolution, as the amplitude of perturbations outside the range bounded by two grey lines remains smaller than that of the initial perturbations. Consequently, relating drag coefficient D to the initial perturbations is justified.

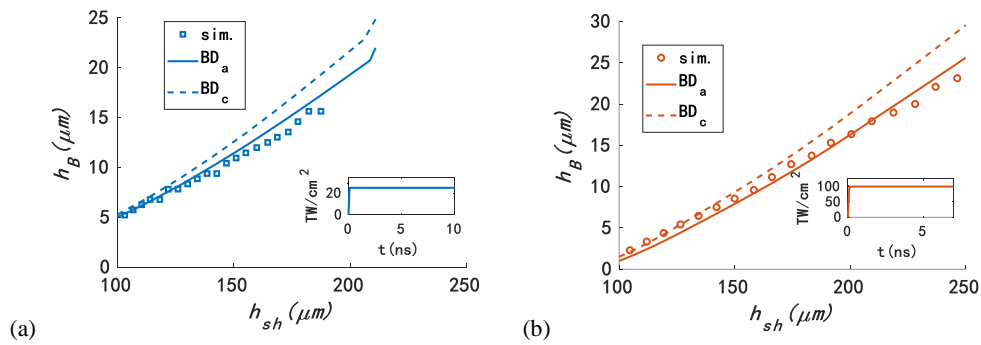


Figure 3. The relationship between h_B and the distance, h_{sh} , traveled by the ablation front that is also the interface between the bubble and the spike for (a): case 1 and (b): case 3. The symbols are obtained from simulations, and the dashed and solid lines are predicted by equation (3) without and with ablation, respectively.

We subsequently validate equation (3), particularly concerning ablative stabilization. h_B predicted by equation (3) without ablation is larger than that obtained from simulations, while the predicted h_B from equation (3) with ablation aligns well with the simulation results under various laser pulses in figure 3(a) and (b). As the distance h_{sh} traveled by the ablation front increases, the effects of accumulated ablative

stabilization become more pronounced.

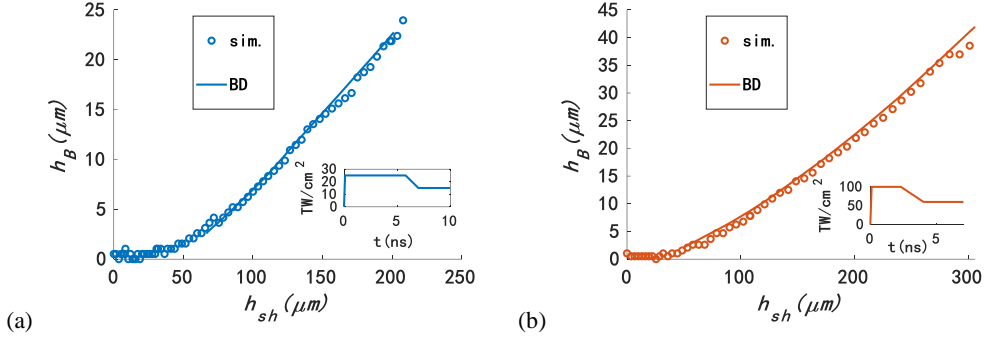


Figure 4. The relationship between h_B and h_{sh} for (a): case 2 and (d): case 4.

While in non-steady situations, the predicted h_B corresponds with the simulation results under two different pulses, as depicted in figure 4(a) and (b). It is evident that equation (2) does not provide better predictions than equation (3) due to the nonlinear relation between h_B and $h_{sh} \sim (\int \sqrt{g} dt)^2$. Additionally, resolution effects introduce errors ($\pm 1.04 \mu m$), leading to reduced confidence in h_B before $h_{sh} \leq 50 \mu m$.

3.3 Sensitivity of the model

The adjustable coefficient D is influenced by the initial perturbations and ablative acceleration history. For the same acceleration g , h_B increases as D decreases due to a reduced drag force. Consequently, we can validate the sensitivities of equation (3) to variations in initial perturbations and γ .

Figure 5(a) illustrates the dependence on $\langle h_{k0} \rangle = v_{k0} / \gamma$, where the onset of nonlinearity is indicated by the beginning of the solid fitting lines. Cases with larger $\langle h_{k0} \rangle$ transition into the nonlinear phase earlier and achieve greater h_B simultaneously. The impact of $\langle h_{k0} \rangle$ becomes increasingly important for longer acceleration times [13], during which bubbles can progress through several generations. This underscores the necessity for stringent $\langle h_{k0} \rangle$ requirements in high compression

ignition schemes.

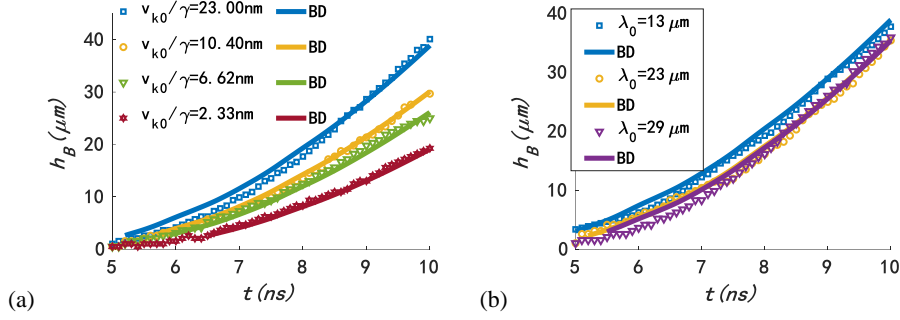


Figure 5. Relationship between h_B and t . (a) with different initial perturbation amplitudes v_{k0}/γ for case 1, 5, 6 and 7; (b) with different initial perturbation wavelengths $\lambda_0 = 2\pi/k_{B,0}$ for case 8-10.

Figure 5(b) presents the dependence on the perturbation wavelengths λ_0 , which remain unstabilized. Cases with shorter λ_0 exhibit larger h_B , indicating that the enhancement of ablative stabilization is weaker than the change of logarithmic term expressed in equation (1). However, the sensitivity diminishes for cases with wavelength differences of less than 6 μm under this simulation settings. This indicates that effective control of ARTI through perturbation wavelength requires exceeding a threshold value in wavelength differences.

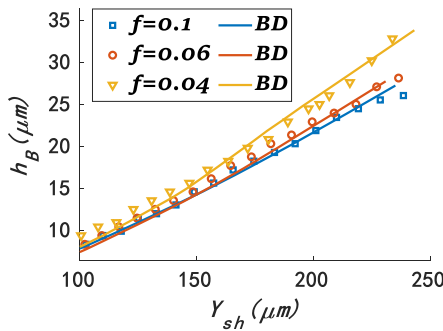


Figure 6. h_B varying with Y_{sh} for case 12, 3 and 11.

To access the sensitivities of ARTI to γ , we modify the magnitude of local heat fluxes near the maximum temperature gradient by adjusting the flux limited value f .

Figure 6 illustrates that until $h_{sh} > 150\mu m$, h_B with different f gradually diverges.

The predicted h_b aligns with the simulation results, increasing as f decreases. If the drag force remains constant, g increasing with f leads to increasing perturbations, which contrasts with the trend observed in figure 6. Thus, the elongation of bubbles at lower f can be contributed to the decreasing drag force with a smaller D , demonstrating that, given sufficient time for evolution, equation (3) is sensitive to variations in γ .

3.4 Control of nonlinear ARTI

Following the validation of the effectiveness and sensitivity of equation (3), we will further explore strategies for controlling nonlinear ARTI. To illustrate this control strategy, we will consider self-similar growth as an example.

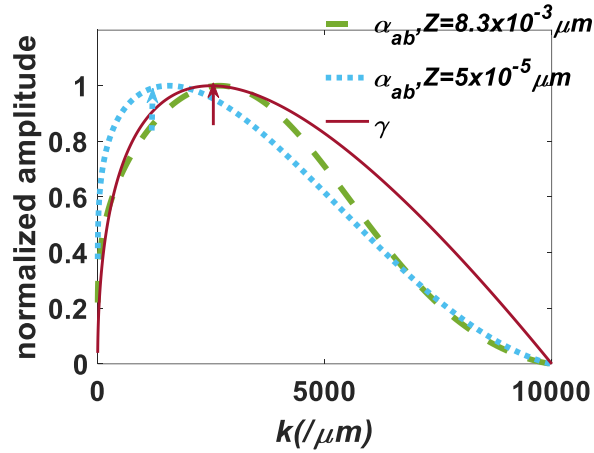


Figure 7. Variation of α_{ab} and γ with k . The arrows represent the “most dangerous mode”. The

initial value is taken as follows: $\beta\sqrt{1/(A_g)}v_a = 10^{-2} \mu m^{1/2}$, $Z = \langle h_{k_0} \rangle / (C\sqrt{\pi})$.

Equation (2) indicates that maintaining α_{ab} , below its maximum value can effectively control self-similar ARTI. In the classical self-similar regime, which is dominated by bubble competition, the self-similar coefficient lacks an extremum due to $\frac{\partial \alpha_b}{\partial k_B} < 0$ [23]. However, $\frac{\partial \alpha_{ab}}{\partial k_B} = 0$ exists within the context of ARTI, leading to the establishment of the “most dangerous mode” k_a characterized by the maximum

α_{ab} . Figure 7 illustrates the normalized amplitudes of α_{ab} and γ varying with k . Different from the “classical most dangerous mode” k_γ , determined by the maximum γ , k_α depends on initial perturbations. Therefore, based on $\langle h_{k0} \rangle$ generated by the current quality of the target and beam, we can strategically control the dominant mode to ensure that it remains far from k_α as case 8 and 9. In the context of target defects or laser imprint, modes that initially exist in the nonlinear phase are unlikely to persist as the dominant mode during the nonlinear phase, as they will not exhibit a self-similar manner. Instead, these modes primarily influence the vorticity, which in turn affects the terminal velocity of λ_0 smaller than $10\mu\text{m}$ [19]. By strategically controlling the shape and amplitude of perturbations, it is possible to displace the dominant mode away from the “most dangerous mode”. This approach may elucidate gain differences among targets of similar qualities and provide guidance for target manufacturing and pulse optimization in the vicinity of the ignition cliff, ultimately achieving a high fusion gain.

4. Conclusions

Prior research has demonstrated that local defects and laser imprint can evolve into a weakly nonlinear, or self-similar phase. In ICF, which typically involves non-steady ablation and various physical mechanisms, we extend the classical buoyancy-drag (BD) model to develop an ablative BD model for evaluating and guiding the control of nonlinear ARTI in real space. The model’s application in the weakly nonlinear phase and self-similar phase is characterized by its innovative expression of D based on initial perturbations, γ and U_B . Following the validation of the effectiveness and sensitivity of equation (3) through radiation-hydrodynamic code FLASH, we utilize the “most dangerous mode” k_α , which depends on initial perturbations, to effectively control nonlinear ARTI. Our findings suggest that k_α may elucidate the differences in

gains among targets of similar qualities and provide valuable guidance for target manufacturing and pulse optimization near the ignition cliff. While previous studies have examined the impact of various target defects on improving target gain, our research offers a potentially unified approach for evaluating and controlling nonlinear ARTI.

Acknowledgements

This work is supported by the supported by the National Key R & D Projects (Grant No. 2023YFA1608402), Strategic Priority Research Program of the Chinese Academy of Sciences (Grant No. XDA25010200), and Nature Science Foundation of China (Grant No. 12375242).

References

- [1] Abu-Shawareb, H., Acree, R., Adams, P., Adams, J., Addis, B., Aden, R., Adrian, P., Afeyan, B. B., Aggleton, M., Aghaian, L., ... and Zylstra, A. B, 2022. Lawson criterion for ignition exceeded in an inertial fusion experiment. *Physical Review Letters*, 129(7), p.075001.
- [2] Abu-Shawareb, H., Acree, R., Adams, P., Adams, J., Addis, B., Aden, R., Adrian, P., Afeyan, B. B., Aggleton, M., Aghaian, L., ... and Zylstra, A. B, 2024. Achievement of target gain larger than unity in an inertial fusion experiment. *Physical Review Letters*, 132(6), p.065102.
- [3] Smalyuk, V. A., Weber, C. R., Landen, O. L., Ali, S., Bachmann, B., Celliers, P. M., Dewald, E. L., Fernandez, A., Hammel, B. A., Hall, G., ... and Stadermann, M., 2019. Review of hydrodynamic instability experiments in inertially confined fusion implosions on National Ignition Facility. *Plasma Physics and Controlled Fusion*, 62(1), p.014007.
- [4] Casner, A., 2021. Recent progress in quantifying hydrodynamics instabilities and turbulence in inertial confinement fusion and high-energy-density experiments. *Philosophical*

Transactions of the Royal Society A, 379(2189), p.20200021.

- [5] Haan, S. W., Lindl, J. D., Callahan, D. A., Clark, D. S., Salmonson, J. D., Hammel, B. A., Atherton, L. J., Cook, R. C., Edwards, M. J., Glenzer, S., ... and Wilson, D. C., 2011. Point design targets, specifications, and requirements for the 2010 ignition campaign on the National Ignition Facility. *Physics of Plasmas*, 18(5), p.051001.
- [6] Lindl, J., Landen, O., Edwards, J., Moses, E. and NIC team, 2014. Review of the national ignition campaign 2009-2012. *Physics of Plasmas*, 21(2), p.020501.
- [7] Hurricane, O. A., Callahan, D. A., Casey, D. T., Celliers, P. M., Cerjan, C., Dewald, E. L., Dittrich, T. R., Döppner, T., Hinkel, D. E., Hopkins, L. B., ... and Tommasini, R., 2014. Fuel gain exceeding unity in an inertially confined fusion implosion. *Nature*, 506(7488), pp.343-348.
- [8] Divol, L., Pak, A., Bachmann, B., Baker, K. L., Baxamusa, S., Biener, J., and Wilde, C. H. 2024. Thermonuclear performance variability near ignition at the National Ignition Facility. *Physics of Plasmas*, 31(10), p.102703
- [9] Pak, A. 2023. Overview of principal degradations arising from capsule target perturbations in inertial confinement fusion implosions (No. LLNL-CONF-854535). Lawrence Livermore National Laboratory (LLNL), Livermore, CA (United States).
- [10] Goncharov, V. N., Gotchev, O. V., Vianello, E., Boehly, T. R., Knauer, J. P., McKenty, P. W., and Cherfils-Clérouin, C. 2006. Early stage of implosion in inertial confinement fusion: Shock timing and perturbation evolution. *Physics of Plasmas*, 13(1), p.012702.
- [11] Liu, D. X., Tao, T., Li, J., Jia, Q. and Zheng, J., 2022. Mitigating laser imprint with a foam overcoating. *Physics of Plasmas*, 29(7), p.072707.

-
- [12] Smalyuk, V. A., Sadot, O., Delettrez, J. A., Meyerhofer, D. D., Regan, S. P., and Sangster, T. C., 2005. Fourier-space nonlinear Rayleigh-Taylor growth measurements of 3D laser-imprinted modulations in planar targets. *Physical Review Letters*, **95**(21), p. 215001.
- [13] Casner, A., Masse, L., Liberatore, S., Loiseau, P., Masson-Laborde, P. E., Jacquet, L., Martinez, D., Moore, A. S., Seugling, R., Felker, S., ... and Nikroo, A., 2015. Probing the deep nonlinear stage of the ablative Rayleigh-Taylor instability in indirect drive experiments on the National Ignition Facility. *Physics of Plasmas*, **22**(5), p.056302.
- [14] Zhang, H., Betti, R., Yan, R., Zhao, D., Shvarts, D. and Aluie, H., 2018. Self-similar multimode bubble-front evolution of the ablative Rayleigh-Taylor instability in two and three dimensions. *Physical Review Letters*, **121**(18), p.185002.
- [15] Zhang, H., Betti, R., Yan, R. and Aluie, H., 2020. Nonlinear bubble competition of the multimode ablative Rayleigh-Taylor instability and applications to inertial confinement fusion. *Physics of Plasmas*, **27**(12), p.122701.
- [16] Martinez, D. A., Smalyuk, V. A., Kane, J. O., Casner, A., Liberatore, S. and Masse, L. P., 2015. Evidence for a bubble-competition regime in indirectly driven ablative Rayleigh-Taylor instability experiments on the NIF. *Physical Review Letters*, **114**(21), p.215004.
- [17] Sadot, O., Smalyuk, V. A., Delettrez, J. A., Meyerhofer, D. D., Sangster, T. C., Betti, R., Goncharov, V. N., and Shvarts, D., 2005. Observation of self-similar behavior of the 3D, nonlinear Rayleigh-Taylor instability. *Physical Review Letters*, **95**(26), p.265001.
- [18] Takabe, H., Mima, K., Montierth, L. and Morse, R. L., 1985. Self-consistent growth rate of the Rayleigh-Taylor instability in an ablatively accelerating plasma. *The Physics of Fluids*, **28**(12), pp.3676-3682.

-
- [19] Betti, R., Goncharov, V. N., McCrory, R. L., Sorokin, P. and Verdon, C. P., 1996. Self-consistent stability analysis of ablation fronts in inertial confinement fusion. *Physics of Plasmas*, 3(5), pp.2122-2128.
- [20] Goncharov, V. N., 2002. Analytical model of nonlinear, single-mode, classical Rayleigh-Taylor instability at arbitrary Atwood numbers. *Physical Review Letters*, 88(13), p.134502.
- [21] Haan, S. W., 1989. Onset of nonlinear saturation for Rayleigh-Taylor growth in the presence of a full spectrum of modes. *Physical Review A*, 39(11), p.5812.
- [22] Haan, S. W., 1991. Weakly nonlinear hydrodynamic instabilities in inertial fusion. *Physics of Fluids B: Plasma Physics*, 3(8), pp.2349-2355.
- [23] Dimonte, G., 2004. Dependence of turbulent Rayleigh-Taylor instability on initial perturbations. *Physical Review E—Statistical, Nonlinear, and Soft Matter Physics*, 69(5), p.056305.
- [24] Baker, L. and Freeman, J. R., 1981. Heuristic model of the nonlinear Rayleigh-Taylor instability. *Journal of Applied Physics*, 52(2), pp.655-663.
- [25] Dimonte, G., 2000. Spanwise homogeneous buoyancy-drag model for Rayleigh–Taylor mixing and experimental evaluation. *Physics of Plasmas*, 7(6), pp.2255-2269.
- [26] Layzer D., 1955. On the instability of superposed fluids in a gravitational field. *Astrophysical Journal*, 122(1), p.1.
- [27] Hansom, J. C. V., Rosen, P. A., Goldack, T. J., Oades, K., Fieldhouse, P., Cowperthwaite, N., Youngs, D. L., Mawhinney, N. and Baxter, A. J., 1990. Radiation driven planar foil instability and mix experiments at the AWE HELEN laser. *Laser and Particle Beams*, 8(1-2), pp.51-71.
- [28] Rana, V., Lim, H., Melvin, J., Glimm, J., Cheng, B., and Sharp, D. H., 2017. Mixing with

-
- applications to inertial-confinement-fusion implosions. *Physical Review E*, **95**(1), p. 013203.
- [29] Huntington, C. M., Shimony, A., Trantham, M., Kuranz, C. C., Shvarts, D., Di Stefano, C. A., Doss, F. W., Drake, R. P., Flippo, K. A., Kalantar, D. H., ... and Park, H. S., 2018. Ablative stabilization of Rayleigh-Taylor instabilities resulting from a laser-driven radiative shock. *Physics of Plasmas*, **25**(5), p.052118.
- [30] Li, J., Yan, R., Zhao, B., Zheng, J., Zhang, H. and Lu, X., 2022. Mitigation of the ablative Rayleigh–Taylor instability by nonlocal electron heat transport. *Matter and Radiation at Extremes*, **7**(5), p.055902.
- [31] Li, J., Yan, R., Zhao, B., Wu, J., Wang, L. and Zou, S., 2024. Effect of hot-electron preheating on the multimode bubble-front growth of the ablative Rayleigh–Taylor instability. *Physics of Plasmas*, **31**(1), p.012703.
- [32] Betti, R. and Sanz, J., 2006. Bubble acceleration in the ablative Rayleigh-Taylor instability. *Physical Review Letters*, **97**(20), p.205002.
- [33] Zhang, D., Li, J., Xin, J., Yan, R., Wan, Z., Zhang, H. and Zheng, J., 2022. Self-generated magnetic field in ablative Rayleigh–Taylor instability. *Physics of Plasmas*, **29**(7), p.072702.
- [34] Walsh, C. A., Chittenden, J. P., McGlinchey, K., Niasse, N. P. L. and Appelbe, B. D., 2017. Self-generated magnetic fields in the stagnation phase of indirect-drive implosions on the National Ignition Facility. *Physical Review Letters*, **118**(15), p.155001.
- [35] Walsh, C. A. and Clark, D. S., 2023. Nonlinear ablative Rayleigh-Taylor instability: Increased growth due to self-generated magnetic fields. *Physical Review E*, **107**(1), p.L013201
- [36] Pak, A., Zylstra, A. B., Baker, K. L., Casey, D. T., Dewald, E., Divol, L., Young, C. V. 2024. Observations and properties of the first laboratory fusion experiment to exceed a target gain of

unity. *Physical Review E*, 109(2), p.025203.

- [37] El Rafei, M. and Thornber, B., 2020. Numerical study and buoyancy–drag modeling of bubble and spike distances in three-dimensional spherical implosions. *Physics of Fluids*, 32(12), p.124107.
- [38] Youngs, D. L. and Thornber, B., 2020. Buoyancy–Drag modelling of bubble and spike distances for single-shock Richtmyer–Meshkov mixing. *Physica D: Nonlinear Phenomena*, 410, p.132517.
- [39] Birkhoff, G., 1955. University of California Report No. LA-1862.
- [40] Peebles, J. L., Hu, S. X., Theobald, W., Goncharov, V. N., Whiting, N., Celliers, P. M., Ali, S. J., Duchateau, G., Campbell, E. M., Boehly, T. R. and Regan, S. P., 2019. Direct-drive measurements of laser-imprint-induced shock velocity nonuniformities, *Physical Review E*, 99(6), p.063208.
- [41] Fryxell, B., Olson, K., Ricker, P., Timmes, F. X., Zingale, M., Lamb, D. Q., MacNeice, P., Rosner, R., Truran, J. W. and Tufo, H., 2000. FLASH: An adaptive mesh hydrodynamics code for modeling astrophysical thermonuclear flashes. *The Astrophysical Journal Supplement Series*, 131(1), p.273.